Chapter 4

Experimental Setup

4.1 Introduction

To measure the electronic spectra of protonated PAHs, appropriate protonation and detection methods need to be selected. In general, protonated PAHs can be produced in a hydrogen discharge of some kind, or by a proton transfer from other protonated molecules. The method for recording the spectrum may strongly depend on the way the protonation has been performed, and so should be considered in tandem with the production techniques.

In afterglow discharge experiments [75], for example, the reactions of PAH cations with hydrogen were studied. As a result of these reactions, the cations of aromatic molecules (benzene, naphthalene and pyrene) acquired hydrogen atoms, making protonated PAHs with nearly 100% efficiency. For this fairly high pressure method, the protonated PAH spectra would have to be recorded in direct absorption. Even with multipass configurations for the laser beam, the sensitivity of such methods is usually low. The absorption strength would strongly depend on the concentration of protonated PAHs, but high concentrations are not easily achievable for multi-ring PAHs due to their low vapor pressures. The sample and possibly the flow cell would therefore need to be heated to increase the amount of absorbing ions, and the high temperatures and collision frequency would broaden the

spectrum significantly.

In the IR cluster photodissociation experiments on $C_6H_7^+$ [3, 96], protonated benzene was created by proton transfer from the H_3^+ produced as a result of H_2 molecule ionization by an electron gun. This method produced protonated benzene that was sufficiently cold to cluster with Ar, N_2, etc. Such a protonation method requires high pressure at the pulsed valve throat which can be achieved by increasing the carrier gas pressure behind the pulsed valve (i.e. the backing pressure) to ∼10 atm. This creates a significant load on vacuum pumps and requires multiple differential pumping stages with good ion guides. It is possible to decrease the gas load on the pumps by shortening the gas pulse duration, but the piezo-based pulsed valves must be used in this case. Piezo valves cannot be heated above 80 – 100 °C and would be useful only when working with benzene and naphthalene, but not larger PAHs.

Alternatively, PAHs may be protonated in a longitudinal pulsed discharge source (pinhole or slit). Discharge sources of this kind have been used successfully to create a wide array of species, including neutral, cationic and anionic carbon chains, and miscellaneous radicals [40, 135–137]. These discharge sources do not require high gas backing pressure and are easy to operate. When heated, they may be used with large PAHs as well, although it must be noted that the ions produced are typically vibrationally warmer than the ones from electron gun ionization-based sources.

A suitable way to record the spectra needs to be selected once the production method is set. Absorption or photodissociation would be the most appropriate methods for the gas phase spectroscopy of positive ions. As mentioned earlier, a typical absorption experiment requires a large number of protonated PAH molecules to be produced, even if some kind of multipass scheme for the light is implemented. The most sensitive of such methods –

cavity ringdown spectroscopy – has been used successfully to record absorption spectra of PAH cations (naphthalene, pyrene) produced in a slit pulsed discharge source [62–64]. It was estimated that with our discharge source, the cavity ringdown method would barely be able to detect any absorption due to the low number of protonated PAH ions and was therefore discarded.

An alternative method would be to conduct photodissociation measurements on protonated ions. Resonance Enhanced Multiphoton Dissociation (REMPD) was used previously to record the electronic spectra of the naphthalene [67], anthracene and phenanthrene [138] cations. Photodissociation was also used for protonated benzene [89,90] as well. The central problem with this method lies in its multiphoton character, therefore either high radiation intensity or long interaction time between the ions and photons are needed.

In our experiments, a longitudinal pinhole pulsed discharge source was used for PAH protonation due to its robustness and compatibility with existing equipment. Laser photodissociation was chosen to record spectra, and a reflectron time-of-flight mass spectrometer was used as a detection method.

4.2 Pulsed Discharge Source

4.2.1 Design

The pulsed discharge source was based on the Thaddeus group design used for the Fourier-transform microwave spectroscopy of carbon chains [40]. It was modified for use with the time-of-flight mass spectrometer, but the electronic circuitry was kept the same. The design for our source is shown in Figure 4.1 (see Appendix B, Figures B.1–B.7 for detailed shop drawings). The discharge source consisted of two electrodes mounted on a Parker General

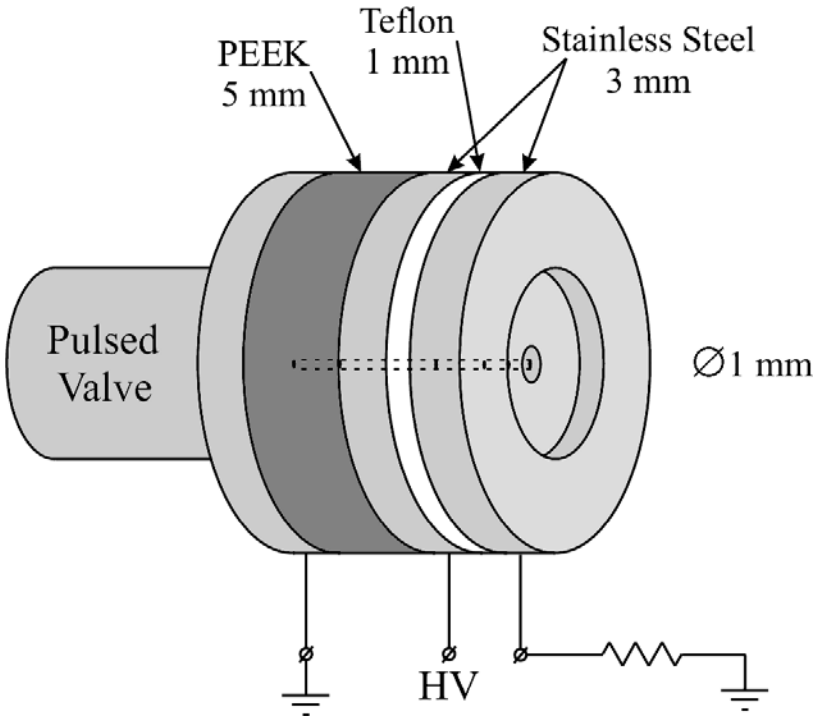

Figure 4.1: The pulsed discharge source design.

Valve series 9 pulsed valve, separated from the valve and each other by insulating spacers. A small channel for the gas flow was drilled in the center of the electrodes and spacers. The diameter of the channel was 1.0 mm. This value was optimized for the best discharge conditions which consisted of balancing the preferably low pressure for the discharge with the preferably high pressure for gas cooling during the expansion into vacuum. The diameter of the pulsed valve orifice was 0.7 mm. To avoid a parasitic volume next to the pulsed valve, the face of the valve body was flat, that is, there was no standard cone around the orifice. The outside diameter of the electrodes and spacers was the same as for the pulsed valve body – 1.33″ (33.9 mm). The spacer between the electrodes was made of teflon and was 1.0 mm thick. The spacer between the pulsed valve and the inside electrode was made of PEEK (poly-ether-ether ketone) to insulate the heated pulsed valve thermally from the rest of the

discharge assembly. Either a 5.0 or 7.0 mm thick spacer was used. Electrodes were made of stainless steel to prevent their sputtering by the discharge. High voltage rated (up to 5 kV) electric wires were attached to the side of the electrodes with 0–80 screws. Ideally, the electrodes should be as thin as possible (down to 0.5 mm) to avoid plasma neutralization by the electrodes. In our case, they were 2.54 mm thick due to the size of wire lugs and screw heads. The middle part of the outside electrode was made 1.7 mm thick and had a 90° cone to improve the quality of the gas jet flow. Electrodes and wires were wrapped with teflon tape to prevent arcing between electrodes outside the discharge channel. The entire assembly was held together with four screws, insulated electrically from the electrodes by teflon inserts and washers.

In principle, high voltage could be applied to both electrodes in the discharge. In order to avoid ion deflection by the electrode potential after the plasma left the discharge, the outside electrode was held at almost ground potential. It was connected to ground with a 10 Ω, 10 W current monitoring resistor. The negative DC high voltage pulse (up to –2.0 kV) was applied to the inside electrode, and the pulsed valve body was grounded. The discharge would occur between the electrodes and not between the inside electrode and the valve body due to the large difference in the thickness of the PEEK and teflon spacers.

The pulsed valve was operated at 5 – 7 Hz repetition rate by a driver circuit (Appendix B, B.2.2) that applied a 400 μs long pulse to open the valve with a setting of 160 – 180 V on the capacitors C_1. After two to three days of continuous operation, the inside channel of the discharge had to be cleaned of a carbonaceous deposit. The need for cleaning was determined by a decline in the ion signal and an increased surface arcing in the discharge.

4.2.2 Voltage and Current Profiles

The negative high voltage pulse was typically applied to the inside electrode 250 μs after opening the pulsed valve. The duration of the high voltage pulse was 1200 μs to cover the full gas pulse delivered by the valve. Typical voltage and current curves for the discharge are shown in Figure 4.2. In this example, a –560 V pulse was applied. In the absence of gas between discharge electrodes (the front and the tail of the pulse), no discharge occurs. When the gas from the pulsed valve reaches the electrodes, the discharge starts, resulting in the high voltage drop and current flow observed. A dim blue glow was observed at

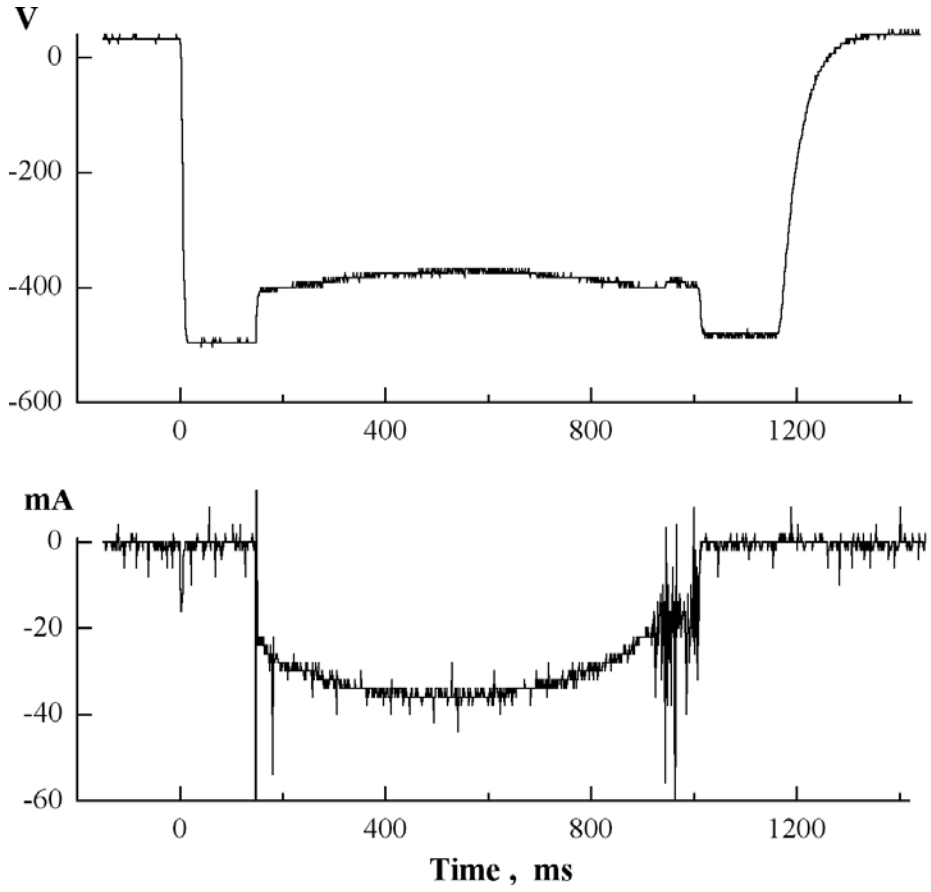

Figure 4.2: Pulsed nozzle discharge voltage and current profiles.

the discharge throat when plasma was expanding into the vacuum chamber of the mass spectrometer. Under these conditions, the discharge is stable and tracks the gas pulse well, as shown in the V(t) and I(t) curves in Figure 4.2.

In the case of an unstable discharge, the discharge start time would fluctuate significantly (by a few hundred microseconds). Sometimes, the discharge would not happen at all when it was 'poisoned' by the carbonaceous deposit inside the channel, or if the concentration of PAH molecules was too high. The latter would happen mostly for C_6H_6. In such cases, the discharge would occur mostly along the surface and not through the gas, resulting in large random spikes in the voltage and current profiles.

4.2.3 Protonation Mechanism and Efficiency

The protonation of PAHs has been performed in discharges with H_2 as the carrier gas (P_{H_2} = 1 – 2.5 atm) and a low concentration of PAH molecules (at their nominal vapor pressure for heated samples). Mass spectra for an anthracene discharge with He and H_2 as carrier gases are presented in Figure 4.3. In He, the discharge produced only anthracene cations (m/z = 178 a.m.u.), and the cation signal was relatively weak. However, when He was replaced with H_2, a cation signal with almost the same strength was produced, along with a new peak at (m/z = 179 a.m.u.) that is much stronger and corresponds to protonated anthracene. The intensity ratio for the protonated and cation mass peaks ranged from 1 : 1 to 20 : 1, with 8 : 1 being a typical value.

The protonation of PAH molecules in the hydrogen discharge was expected to happen through the mechanism of proton transfer from H_3^+ [3]:

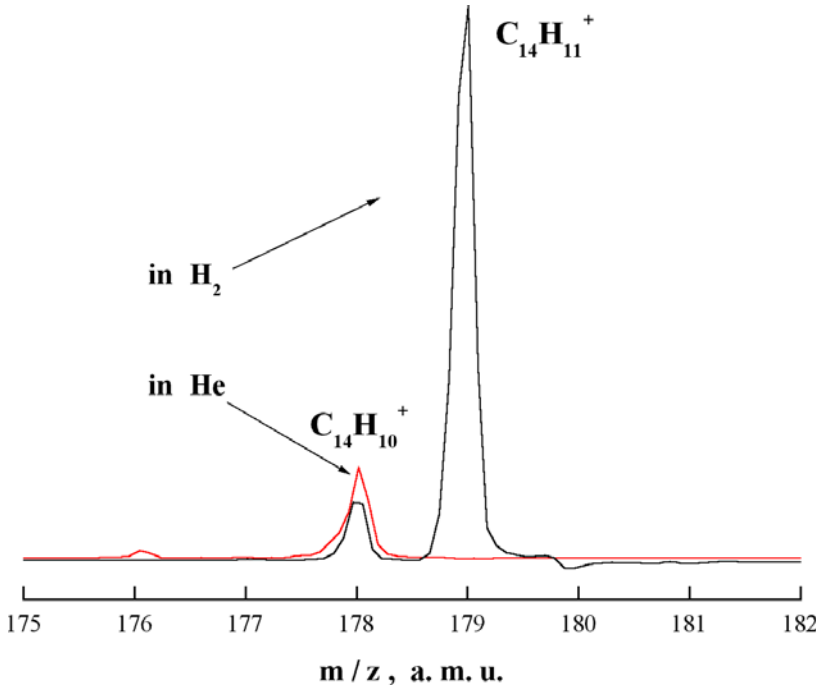

Figure 4.3: Mass spectra of anthracene and protonated anthracene in He *vs.* H_2 discharges.

$$\begin{cases} H_2 + e^- \longrightarrow H_2^+ + 2e^- \\ H_2^+ + H_2 \longrightarrow H_3^+ + H \\ H_3^+ + \text{PAH} \longrightarrow \text{H-PAH}^+ + H_2 \end{cases}$$

Indeed, in the mass spectrum of a pure H_2 discharge, the following mass peaks were observed: H^+, H_2^+ and H_3^+ (m/z = 1, 2 and 3 a.m.u. in Figure 4.4).

The threshold voltage for the discharge to start was –800–900 V in pure H_2. Whenever PAH molecules were added into the discharge, that value dropped to –530–560 V. Simultaneously, the H_3^+ peak disappeared from the mass spectrum. One explanation for this behavior would be that all the H_3^+ ions were scavenged by PAH molecules. However, a more realistic mechanism for PAH protonation is likely via PAH ionization by discharge electrons, followed either by association with H atoms or by PAH cation hydrogen abstraction from the H_2 carrier gas:

$$\begin{cases} \mathrm{PAH} + e^- \longrightarrow \mathrm{PAH}^+ + 2e^- \\ \mathrm{PAH}^+ + \mathrm{H} \longrightarrow \text{H-PAH}^+ \end{cases}$$

$$\begin{cases} \mathrm{PAH} + e^- \longrightarrow \mathrm{PAH}^+ + 2e^- \\ \mathrm{PAH}^+ + \mathrm{H_2} \longrightarrow \text{H-PAH}^+ + \mathrm{H} \end{cases}$$

This would easily explain the threshold voltage drop, and the first process is known to be fast [75]. The second was not observed at room temperature due to a barrier in the hydrogen abstraction reaction, but may be possible at higher temperatures in the discharge, or with internal excitation of the PAH.

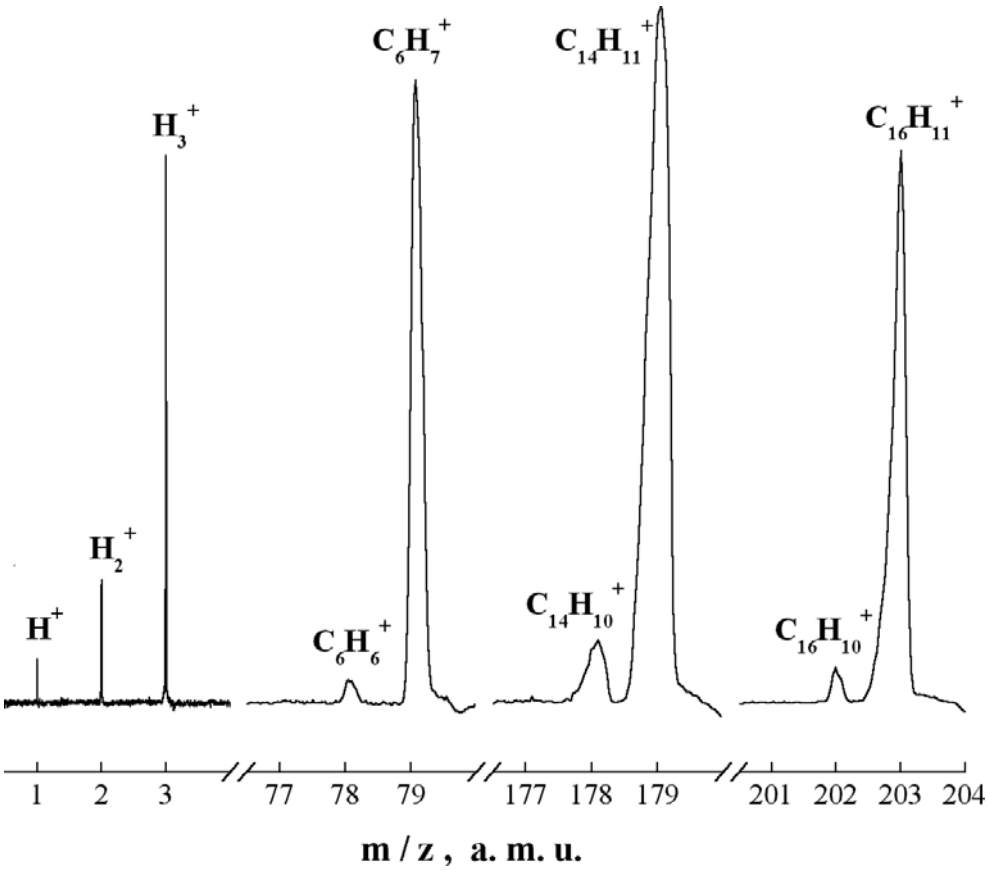

Figure 4.4: H_3^+ formation and the protonation of different aromatic molecules (benzene, anthracene and pyrene) in hydrogen discharges.

The protonation of benzene, anthracene and pyrene has been optimized in a discharge (Figure 4.4). In the case of anthracene and pyrene, $\sim$5 – 10 g of the crystalline solid (Aldrich, 99% purity) was placed into an aluminium sample holder tube and connected to the pulsed valve with stainless steel tubing, with carrier gas (H_2) supplied to the tubing as well. The pulsed valve and sample holder were placed in thermal contact with, and heated by, electric heating cartridges. The stainless steel tubing was heated by heating tape wrapped around it. Temperatures were measured by K-type thermocouples and controlled by temperature controllers (Omega 7600CN). Typical temperatures used in the experiments were:

$$T_{sample} = 130\ ^\circ C,\ \ T_{tubing} = 137\ ^\circ C,\ \ T_{valve} = 145\ ^\circ C \ \text{ for anthracene; and}$$

$$T_{sample} = 168\ ^\circ C,\ \ T_{tubing} = 174\ ^\circ C,\ \ T_{valve} = 180\ ^\circ C \ \text{ for pyrene.}$$

The pulsed valve was kept 15 °C warmer than the sample to reduce sample recrystallization on the inside of the valve faceplate due to its cooling from the gas flow into vacuum.

For protonated benzene, $\sim$10 – 20 mL of benzene were placed into a stainless steel container and hydrogen was bubbled though it. For such an operation, the high concentration of benzene sometimes caused discharge instability. To reduce this instability, the walls of the gas line tubing were passivated with benzene for $\sim$10 minutes and then the bubbler was disconnected. The passivated benzene evaporated slowly and sustained a stable signal for 1 – 2 hours, after which the procedure was repeated.

The signal produced from protonated PAHs was quite strong. For example, 10^5 protonated anthracene ions per shot were estimated to be detected in the mass spectrometer. The high ion density led to noticeable broadening of mass peaks, thereby reducing the mass resolution. However, the deterioration of mass resolution was not an issue for the ions studied.

4.3 Cluster Source

4.3.1 Design

The cluster source used for making clusters of protonated anthracene with water consisted of the discharge source described above and another pulsed valve for delivering cluster partner molecules (Figure 4.5, see Appendix B, Figures B.3–B.10 for the drawings). The

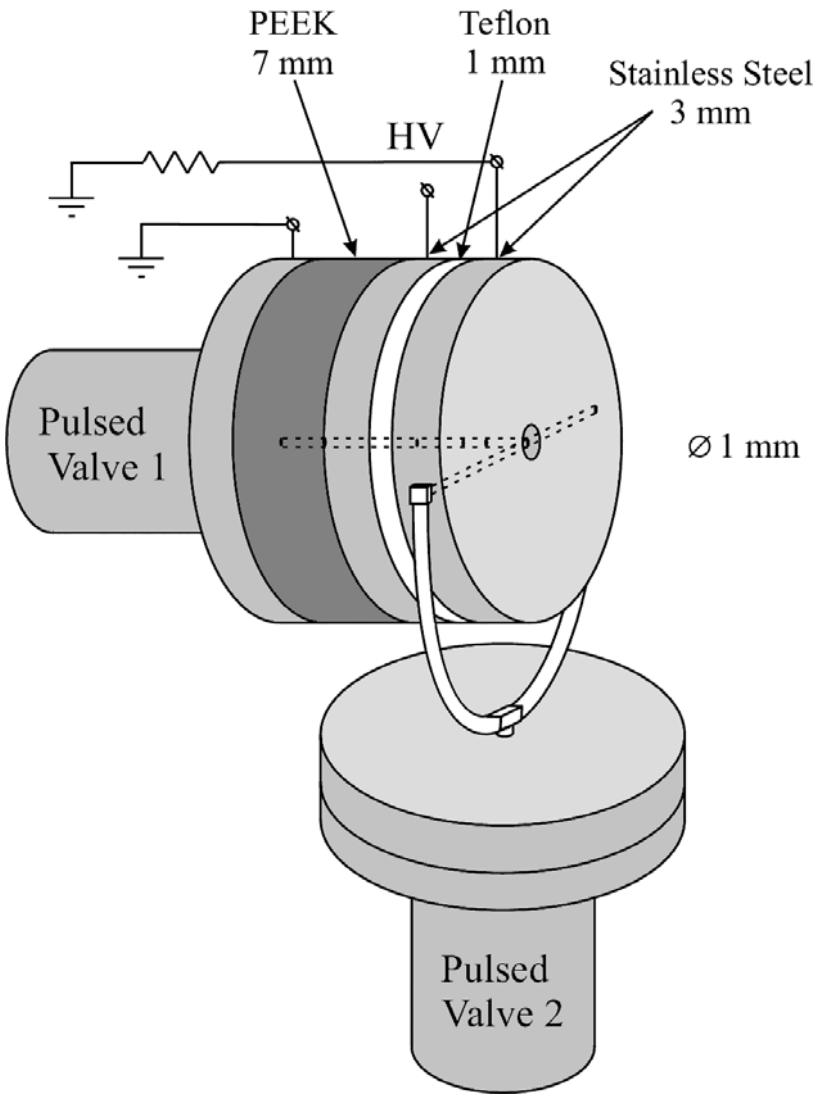

Figure 4.5: Pulsed discharge cluster source with two pulsed valves.

outside electrode of the discharge was modified to be 3 mm thick and had the same thickness in the middle and on the outside. A long 1.0 mm diameter channel was made in the middle of the electrode parallel to the disk plane, crossing the discharge channel at a right angle. The second valve was used for delivering atoms or molecules to create clusters at the discharge exit. Such a design was intended to prevent cluster partner molecules from entering the discharge. On the other hand, clustering occurs most efficiently in high gas pressure regions so clusters must be made at the discharge exit. In our case, PAH molecules are first protonated in the discharge, and as they are about to expand into vacuum, they collide with other molecules.

The second pulsed valve (Parker General Valve series 9) was placed as close as practical to the discharge. It had a faceplate adapter for a gas line. The adapter was equipped with a T-shaped nylon fitting. Similarly, the L-shaped elbow fittings were placed on the side ends of the discharge. Teflon tubing with a $1/16''$ inner diameter connected the fittings in a 'stethoscope' configuration. When the valve was open, the gas would flow through that tubing and enter the discharge region symmetrically from the opposing sides, thus maintaining the pointing of the gas jet.

It should be pointed out that this source is different from another ion cluster mixing source [139], in which clusters of molecular anions with rare gas atoms are first formed in the high pressure expansion. Cluster ligands are then substituted with another molecule in a low pressure cell, filled by the opening of a second pulsed valve.

4.3.2 Operation

Both pulsed valves of the cluster source were operated at a 0.9 Hz repetition rate, limited by the pumping speed available in the mass spectrometer chamber. At higher repetition

rates, the pressure in the flight tube of the time-of-flight mass spectrometer was above 10^{-6} Torr, which could potentially damage the MCP detectors. When photodissociation spectra of clusters were recorded, the laser had to be operated at 10 Hz. To reduce the operating repetition rate for the pulsed valves, a TTL frequency divider circuit (Appendix B, B.2.4) was used with a dividing ratio of 11 : 1.

The second pulsed valve must be opened before the discharge valve, since time is needed for the gas to reach the mixing region of the discharge. Delay times were optimized for the maximum cluster signal by 2–D scanning of the delays between the two pulsed valves, and between the valves and the ion extraction pulse in the mass spectrometer.

4.4 Mass Spectrometer

A Wiley-McLaren time-of-flight mass spectrometer (TOF MS) [140] with a reflectron [141, 142], manufactured by R.M.Jordan Co., was used to detect and analyze positive ions from the discharge (Figure 4.6). It was previously described in detail [143, 144]. The mass-spectrometer chamber consisted of three independently pumped regions for differential pumping. The first chamber was designed to house the pulsed valve, while the second chamber was designed for ion extraction. The skimmer between the first and second chambers was removed in order to move the discharge as close to the extraction ion optics as feasible. The ion optics were enclosed in an extension of a third chamber and were connected to the second chamber via a skimmer (Beam Dynamics, 1 mm diameter) from the discharge side and an orifice (8 mm diameter) on the opposite side to provide an exit for the molecular beam. The third chamber served as the field free ion flight tube. The reflectron was placed close to the end of the flight tube. Microchannel plate (MCP) detectors were placed at both ends of the flight tube to detect ions in the linear and reflectron operation modes of

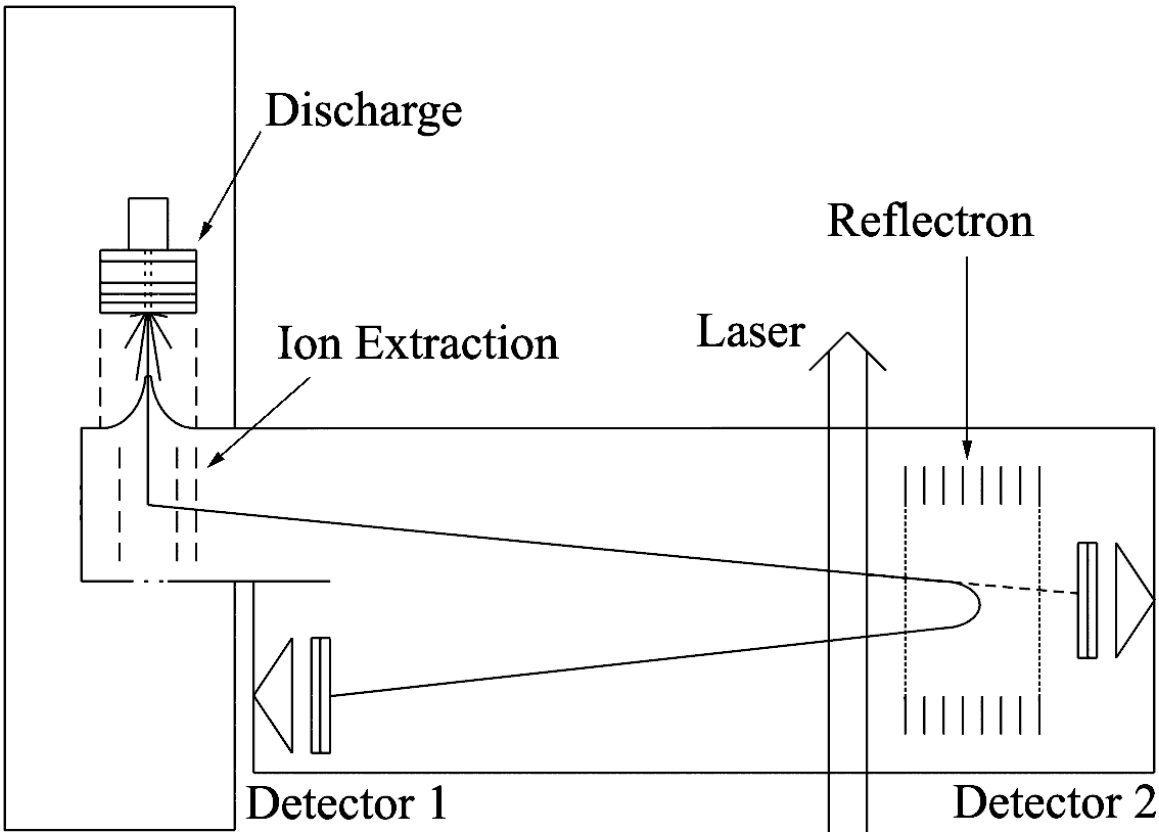

Figure 4.6: The time-of-flight mass spectrometer setup for photodissociation experiments (top view).

the mass-spectrometer.

4.4.1 Ion Shielding

Electrically neutral plasma exited the discharge at almost the thermal supersonic jet velocity, for which the kinetic energy of ions was estimated to be 0.1 eV. Special precautions had to be taken to protect such slow ions from any stray and static voltages inside the chamber.

The discharge source needed to be located as close to the skimmer as possible, and was placed 15 mm from the skimmer. A grounded wire mesh cylinder (1.3″ diameter) was placed around the supersonic jet along its path to the skimmer. Wires that delivered high

voltage to ion optics were ground shielded whenever possible.

All of these measures were not enough, however, since the discharge plasma was creating surface charges on the skimmer and mesh surfaces. To improve the conductivity of the metal surfaces, the face of the discharge source, the skimmer, and the wire mesh were coated with carbon black film (Acheson Aquadag paste dissolved in acetone). This improved the detected ion signal dramatically and enabled ion extraction from any part of the discharge pulse.

4.4.2 Ion Extraction

Positively charged ions were pushed by a repeller grid A_1 (at 3150 V) to an extraction grid A_2 (at 2850 V), and then accelerated to the grounded grid in the direction perpendicular to the molecular beam. An Eisnel lens (at 120 V) was used to focus the ion beam, while two XY deflector plates (typically, at 75 – 120 V) were used to accelerate ions in the horizontal direction parallel to the molecular beam to guide the ion beam onto the MCPs.

When the mass spectrometer was operated in the linear mode, the reflectron was kept at ground potential. In the reflectron mode, reflectron voltages were set to 1900 V and 3300 V, respectively. Voltages on the repeller and the extractor could be static when working with a neutral molecular beam and creating ions by photoionization. When working with ions created in the discharge source, these grids must first be grounded to allow unaccelerated plasma to enter the space between the repeller and the extractor. High voltages must then be applied simultaneously to these grids by a two-channel pulser, described in Appendix B, B.2.3.

High voltages for the ion optics and reflectron MCP detector were provided by a R.M.Jordan AREF power supply (5 kV, 1 mA maximum), for the Eisnel lens by a Hewlett–

Packard 6525A power supply, and for the linear MCP detector by a Stanford Research Systems PS325 power supply, equipped with a voltage divider.

4.4.3 Reflectron Mode

The mass spectrometer was operated in the reflectron mode when photodissociation experiments were performed for two reasons. First, the reflectron helped to improve the mass resolution. For example, the TOF peaks from anthracene cation (178 a.m.u.) and protonated anthracene (179 a.m.u.) produced in the discharge were only partially resolved in the linear mode. In the reflectron mode, they were separated by at least the peak's full width at half maximum (Figure 4.4). The mass resolution in the mass spectrometer depended on the ion density and was lower for ions created by the discharge as compared to the photoionization. When the cluster discharge source was used for making ions, the ion density was lower and the mass resolution was therefore higher.

Second, the use of the reflectron in the photodissociation experiment gave the ability to monitor both parent ion signal depletion and neutral product formation. In the absence of the laser beam, all ions were turned by the reflectron to the reflectron MCP (detector 1). In the photodissociation experiment, the laser beam intercepted the ions before they entered the reflectron. When the ions absorbed laser radiation and dissociated, at least one ion and one neutral product were formed. The ions would still be turned by the reflectron, but the neutral photodissociation product would strike the linear MCP (detector 2). The depletion of the parent ion peak and possibly, the formation of the ion product would be observed with the reflectron detector. The signal-to-noise ratio on detector 1 was fairly poor, since the low dissociation yields could be buried in the intensity fluctuations of the parent ion peak.

On the other hand, the neutral product channel provided a good alternative to ion channel detection. The velocity of the neutral product would be close to the original velocity of the parent ion which had ∼3.0 keV kinetic energy. Thus, the neutral product retained sufficient kinetic energy to produce a measurable signal on the linear detector. Unlike the signal on the reflectron detector, the neutral product signal had very little background and thus a much better signal-to-noise ratio.

4.4.4 Detectors

Each TOF MS detector consisted of two stacked Galileo MCPs. The diameter of the MCPs was 25 mm for the linear detector and 50 mm for the reflectron detector. The gain was regulated by applying up to 1000 V voltage to each MCP. The signal was collected by a conical electrode and sent to a preamplifier. The amplified signal was read by a digital oscilloscope. An EG&G ORTEC 9301 fast preamplifier (gain 10, ±0.7 V output range) was used with the linear detector, while an EG&G ORTEC VT120C fast-timing preamplifier (gain 20, 0 to –5 V output range) was used with the reflectron detector.

4.4.5 Vacuum System

The first chamber was pumped by a 10″ Varian VHS–10 diffusion pump (Dow Corning 705 oil); the second chamber was pumped by a 6″ Varian VHS–6 diffusion pump (Santovac–5 oil); and the flight tube was equipped with a 4″ Edwards Diffstack 100 diffusion pump (Santovac–5 oil). The 10″ and 6″ pumps were baffled by water-cooled baffles, and the 4″ pump had a built-in baffle. Each pump had gate valves on both the intake and exhaust ports. The diffusion pumps were backed by an Edwards EM2-275 mechanical pump.

The pressure in the TOF MS chambers was measured by three MKS cold cathode

pressure gauges, and the backing pressure was measured by a MKS Pirani pressure gauge. With the pulsed valves off, the residual pressure in the chambers was $5{\cdot}10^{-6}$ Torr, $3{\cdot}10^{-7}$ and $2{\cdot}10^{-8}$ Torr, respectively. The backing pressure was $2{\cdot}10^{-3}$ Torr. With the pulsed valve on, the pressure in the second chamber was $6{\cdot}10^{-5}$ Torr and in the flight tube $1{\cdot}10^{-6}$ Torr. Under operating conditions the backing pressure rose to $6{\cdot}10^{-3}$ – $1{\cdot}10^{-2}$ Torr.

The diffusion pump cooling water was supplied by a closed loop Neslab Coolflow System II Liquid/Liquid recirculator. The mechanical pump was cooled by a Neslab Coolflow CFT–75 refrigerated recirculator.

The system was equipped with an interlock circuit (Appendix B in [143]) that was used to monitor the water flow through diffusion pumps and the backing pressure (set to be below 0.1 Torr). When tripped, it would turn off diffusion pump heaters, close pneumatic gate valves between mass spectrometer chambers and diffusion pumps, and turn off the high voltage power supplies connected to the ion optics and MCP detectors.

4.5 Laser Systems

4.5.1 Excimer Laser

A Lambda Physik LPX–120i excimer laser with NovaTube technology was used to generate UV radiation at 193 and 248 nm. The maximum pulse energy was 200 mJ for a 25 $\times$ 9 mm beam. The beam was passed through a 9 mm pinhole, retaining 25% of the original pulse energy, then guided with a system of 193 nm dielectric-coated mirrors into the TOF MS chamber. The size of the clipped, unfocused beam inside the flight tube was set to 10 $\times$ 15 mm for better spatial overlap with the ion cloud. The pulse energy was adjusted by the discharge voltage in the laser. The laser was triggered externally and synchronized with

the pulsed valve.

A mixture of 0.22% F_2, 8.33% Ar, 4.12% He and 87.33% Ne at a total pressure of 3000 mbar was used to produce $\lambda = 193$ nm, while the $\lambda = 248$ nm pulses were produced in a mixture of 0.19% F_2, 4.84% Kr, 3.68% He and 91.29% Ne at the total pressure of 3300 mbar.

4.5.2 Nd:YAG Lasers

Two nanosecond Nd:YAG lasers were used to pump the OPOs. Both lasers were triggered by an external delay generator to provide synchronization with the experiment. The first, a Coherent Infinity 40–100, had a 4.5 ns long pulse and a singe mode beam profile ∼5 mm in diameter. Its frequency was tripled to 355 nm and operated at the maximum energy of 225 mJ/pulse at the fundamental wavelength (1064 nm) to yield 100 mJ/pulse in the third harmonic. The repetition rate of the laser could be adjusted from 0.1 to 100 Hz at 0.1 Hz increments without significant change in the beam profile or pulse energy.

The second Nd:YAG laser, a Spectra–Physics Quanta–Ray GCR–16S, had a 12 ns long pulse and a beam ∼7 mm in diameter. The maximum used pulse energy in the third harmonic (355 nm) was 135 mJ. Although the laser repetition rate could be adjusted from 0 – 15 Hz, the optimal frequency was 10 Hz. The pulse energy would drop noticeably when the repetition rate was changed more than ±1 Hz from that value due to variations in thermal lensing.

4.5.3 BBO Type II OPO

A simple type II β–BaB_2O_4 (BBO) optical parametric oscillator (OPO) described in detail previously [144–146] was used to perform some initial experiments. Two identical

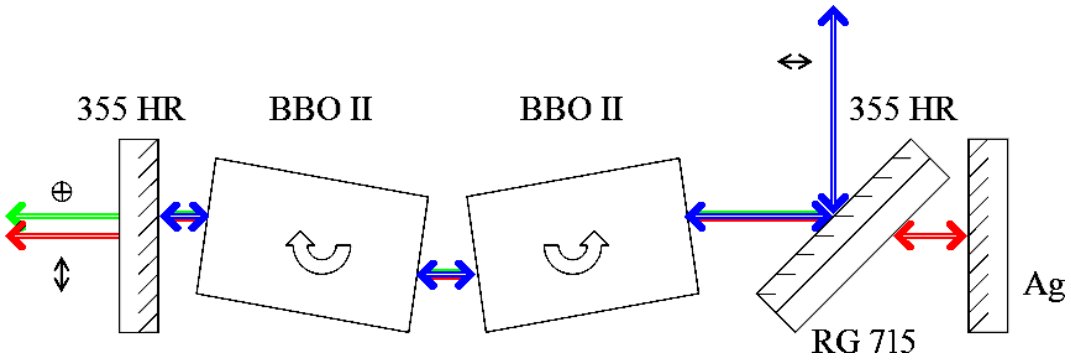

Figure 4.7: A top view of the BBO type II OPO.

type II BBO crystals (6.3 × 12.2 × 12.1 mm, $\Theta = 36°$, $\phi = 45°$) were used in the counter-rotating configuration (Figure 4.7). The OPO cavity, formed by a silver-coated mirror and an output coupler coated with a 355 nm high reflective (HR) coating, was pumped at 30° by the third harmonic of the Coherent Infinity Nd:YAG laser. A long wavelength pass filter (Schott Glass Technologies, RG715) behind a 45° 355 nm HR mirror was used to absorb the visible (signal) wave, but allowed the IR (idler) wave to resonate.

The working wavelength range for the signal wave was 418 – 630 nm. When it was necessary to employ tunable UV radiation, the signal beam was frequency-doubled in a type I BBO crystal (10.0 × 7.0 × 6.1 mm, $\Theta = 56°$, $\phi = 0°$). A Pellin–Broca fused silica prism was used to separate the second harmonic beam from the rest (signal, idler and residual pump). The usable wavelength range for the second harmonic (at least 0.2 mJ/pulse) was 212 – 280 nm.

Both OPO crystals, the second harmonic crystal, and the prism were placed on rotation stages driven by Newport 850F series linear actuators, controlled by the BGSpecT software (Appendix C) via Precision MicroControl DCX–PC100 or DC2–PC100 motion control boards.

4.6 Hybrid BBO OPO with a Rotated Prism Cavity

The OPO described above is robust and simple in operation, but it has a few drawbacks. Most significantly, the OPO conversion efficiency is low when approaching the degeneracy point (2λ or 710 nm for 355 nm pumped OPOs). Indeed, very little or no energy is produced by the type II OPO in the 640 – 800 nm wavelength range. This problem is due to the optical properties of the type II BBO crystals and could, in principle, be solved by replacing the type II BBO with some other crystals – for example, a type I BBO – but doing so would generate new problems.

Another issue is the beam shape. In the blue part of the signal spectrum (420 – 460 nm), the beam is nicely round. At longer wavelengths, however, the beam divergence increases in the non-dispersive direction and the beam profile elongates up to a 7 : 1 aspect ratio. This problem is inherent to such a simple cavity design. To circumvent this behavior, image-rotating OPO cavities have recently been implemented [147,148] that incorporate prisms to rotate the image and waveplates to compensate for the phase mismatch introduced. These image-rotating cavities produce beams of nearly round shape, even at wavelengths where the non-rotating cavities have highly elongated beam profiles. The cavity design in [147] is similar to the simple type II BBO OPO (4.5.3) in that it is also a 355 nm pumped type II BBO OPO with only one crystal. It utilizes the same double pass pump scheme, but instead of the metal-coated mirror, it uses a right angle prism rotated at $\alpha = 45^\circ$ in a back reflector geometry. A $\lambda/2$ waveplate was placed into the cavity to maintain the polarization of the signal wave. Such a design solves the beam profile issue, but not the efficiency around the degeneracy point. In addition, the waveplate has to be rotated as the wavelength is tuned.

To further improve the performance of the OPO, the cavity of the simple type II BBO

OPO was modified as described below.

4.6.1 New Cavity Design

The new cavity design is shown in Figure 4.8. In a similar fashion to the image-rotating cavity [147], the metal-coated mirror in the old cavity was replaced with a fused silica right angle prism. The difference was that the back sides of the prism were coated with aluminium to change the phase rotating properties of the prism. Two BBO crystals were used in the new OPO: one type II and one type I. No waveplates were used and the long wavelengths pass filter was retained to resonate the idler.

The new design may at first seem to be not very logical, but in fact, it has some advantages. Let us take a closer look at its operating principles.

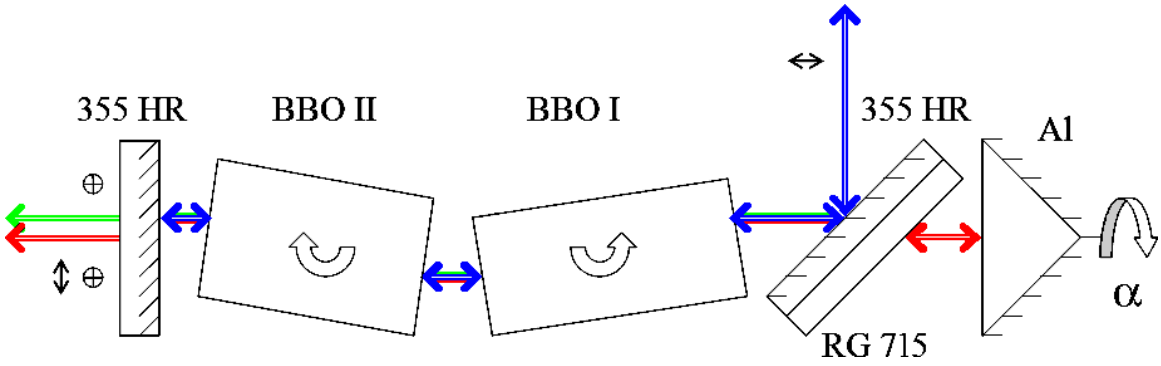

Figure 4.8: A top view of the BBO type I and II hybrid OPO with rotated prism cavity.

4.6.2 Phase Matching

The prism in the cavity introduces a new phase delay to the idler wave. When only the geometric image rotation is considered (Figure 4.9), the general expression for the wave polarization of the original S and P polarized light during prism rotation by α degrees is:

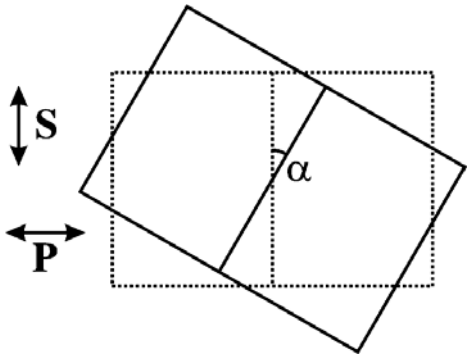

Figure 4.9: A rotated right angle prism.

$$\text{Polarization Rotation} = \begin{cases} 90°(1 + cos(2\alpha)) & , \quad \text{for P polarization} \\ 90°(1 - cos(2\alpha)) & , \quad \text{for S polarization} \end{cases}$$

If the prism is not rotated (its 90° angle edge is parallel to the crystal rotation axis), the image is mirrored in the vertical plane. When the prism is rotated 90°, the image is mirrored in the horizontal plane. At $\alpha = 45°$, both the S and P polarizations are rotated by 90°.

Another factor is the phase delay due to reflections on the prism surfaces. This delay is zero for the non-coated prism and 180° per each internal reflection for the metal coated prism. Delays from the prism refractive index wavelength dependence must also be considered. The overall phase change due to these factors combined is shown in Figure 4.10 for the example of an Al-coated BK–7 glass right angle prism. In the operational range of the OPO, the delay for P polarization is 335 – 350 degrees, which is close to the needed 360° phase shift. For S polarization, it is close to 180 degrees (mirror imaging).

When the prism is rotated by $\alpha = 45°$, the net effect is a 90° polarization rotation with almost complete phase matching. It it possible to achieve better phase matching by slightly rotating the prism. Thus, there is no need for the waveplate. The analysis would change if

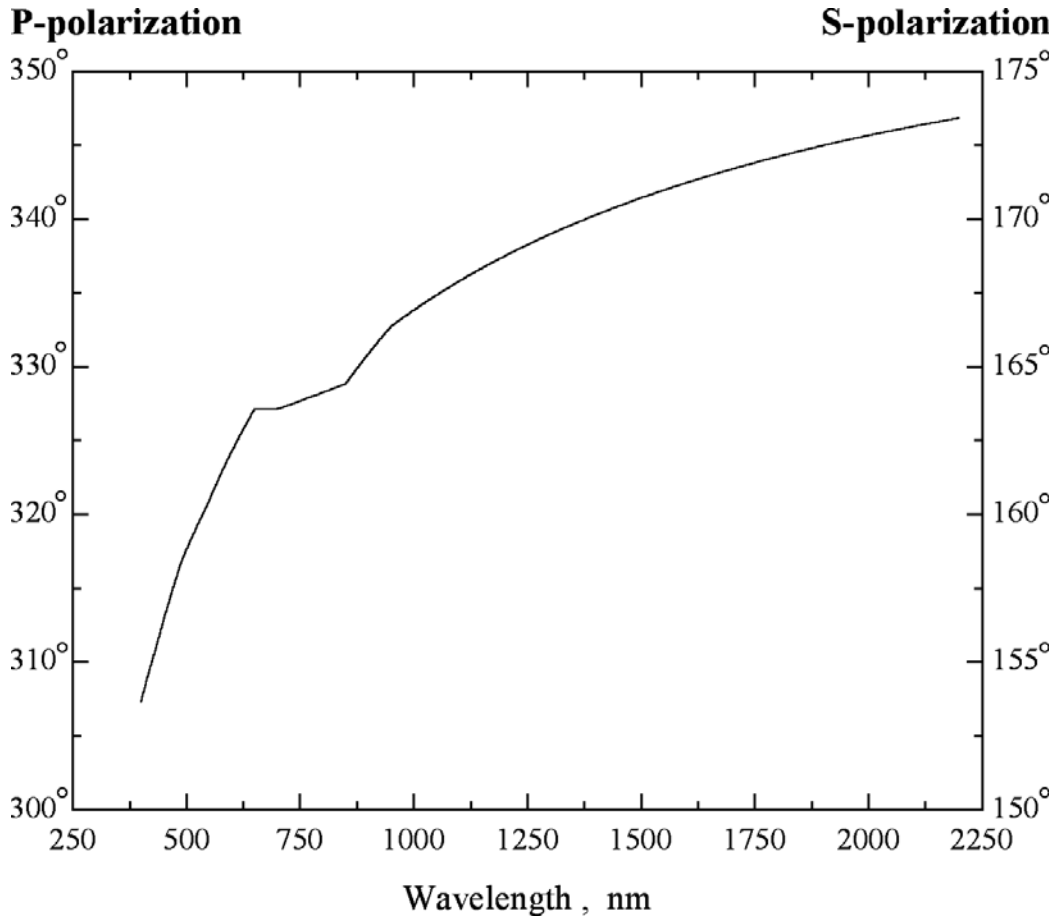

Figure 4.10: The additional phase delay caused by an Al-coated BK–7 right angle prism. Calculated by Foreal Spectrum Co.

the prism were not coated or if the signal wave was resonated.

A polarization rotation of 90° makes the wave unusable for the next pass through the *same* crystal. This may be circumvented by the careful selection of OPO crystals, as described next.

4.6.3 The Choice of Crystals

Crystals used in OPOs must be able to match the group velocities for the pump and signal/idler waves. This is easily achieved in birefringent crystals. For the radiation propagating in such crystals, the polarization has two components (Figure 4.11). The ordinary

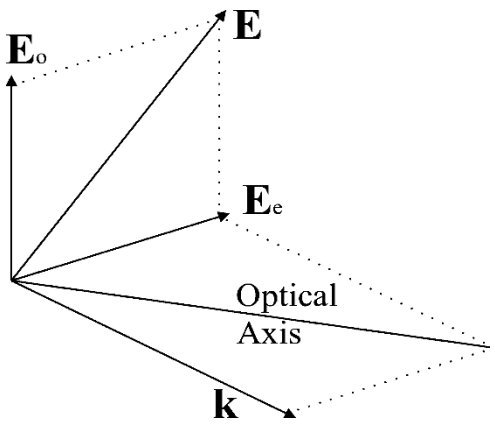

Figure 4.11: Light polarizations in a birefringent nonlinear crystal.

polarization is normal to the plane, formed by the light k–vector and the crystal optical axis, and the extraordinary polarization is in that plane. The refractive index of the ordinary wave does not depend on the angle between the k–vector and the optical axis, but the refractive index of the extraordinary wave does depend on it.

The proper OPO polarizations for BBO crystals are shown in Table 4.1. For both type I and type II BBO, the signal wave polarization is perpendicular to the pump wave polarization, but the idler polarization varies with the crystal type – a fact we exploit in our image/polarization rotating cavity. For the old, non-rotating cavity, the best performance could be achieved only when crystals of the same type are used. For the rotated prism OPO, however, when there are crystals of both types in the cavity, the idler polarization is rotated after each pass and is sequentially amplified by one of the crystals.

Table 4.1: OPO wave polarizations for BBO type I and II crystals.

Wave	BBO I	BBO II
Pump	e	e
Signal	o	o
Idler	o	e

This new OPO, with both BBO type I and type II crystals housed in the cavity, inherits

many of the advantages of each crystal. BBO type I, for example, has better performance around the degeneracy point and a better overall conversion efficiency compared to type II crystals. Hence, in our cavity it serves as the main amplifying crystal. Alternatively, BBO type II has higher $d\lambda/d\Theta$, which means a smaller acceptance angle and narrower bandwidth. In our cavity it therefore serves as a bandpass filter for the type I crystal.

Thus, the new cavity is expected to have a much better beam profile (due to the image rotation by the prism) with as good a linewidth as the old BBO type II only OPO (BBO type II filtering), much better performance around the degeneracy point, and perhaps, higher pulse energy (BBO type I gain).

4.6.4 Hybrid Cavity Performance

The performance of the new OPO has been characterized for $\alpha \simeq 45^\circ$ rotation of the prism. The beam shape in the blue part of the signal wave spectrum is unchanged and circular. In the red part of the signal spectrum, the beam has a shape of the cross with nearly all of the energy concentrated in a small spot at the center of the beam (Figure 4.12). This is similar to the beam shapes from other image-rotating cavities. The measured beam divergence is $\leq$3 mrad at 2 m.

The signal wave was linearly polarized in the direction perpendicular to the pump polarization, which is the same as in the old cavity. The idler wave, however, was elliptically polarized. Thus, the efficiency of the OPO depended on the prism rotation angle α. When it was set to exactly 45°, the pulse energy dependence *vs.* wavelength was similar to the old BBO type II cavity. The pulse energy maximized at 435 nm and steadily dropped as the wavelength was tuned to the red. This behavior most likely resulted from incomplete phase matching. To alleviate this problem, the prism was rotated to $\alpha \simeq 30 - 35^\circ$, which

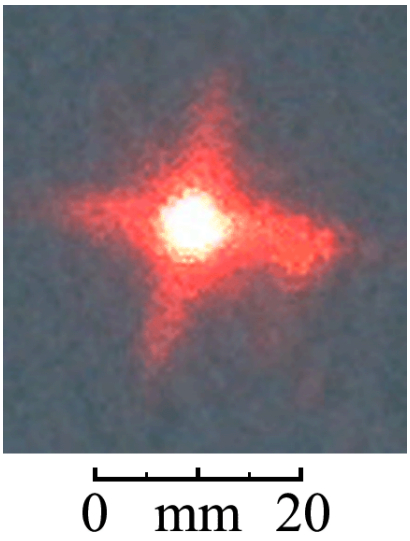

Figure 4.12: Beam shape for the mixed BBO type I and II prism cavity OPO.

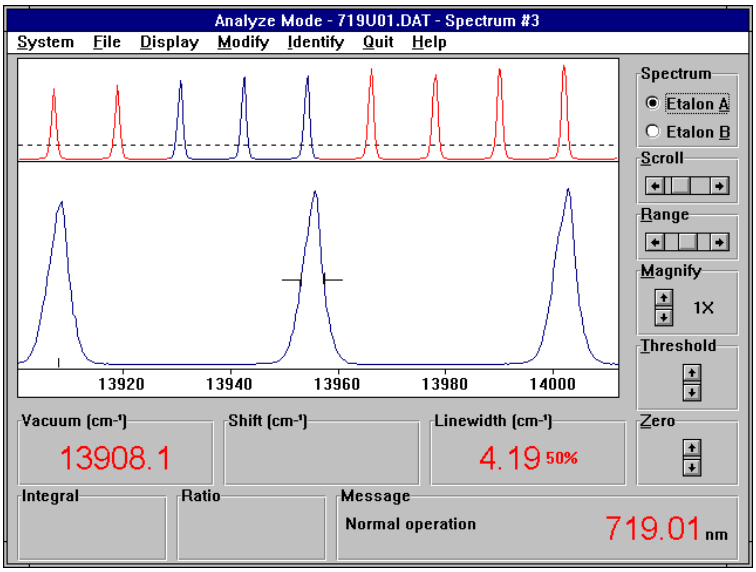

Figure 4.13: Hybrid cavity OPO wavemeter reading at $\lambda_{\text{idler}} = 719$ nm.

drastically improved the efficiency near the degeneracy point. Indeed, tuning to signal wavelengths as long as 710 nm was straightforward, with good efficiency in both the signal and idler beams. Furthermore, the linewidth did not deteriorate significantly around the

degeneracy point as is seen in type I OPOs. The idler wave linewidth at 719 nm was ∼4 cm^{-1} (Figure 4.13), for example, which is close to the 2 – 3 cm^{-1} measured for the signal wave linewidth far from the degeneracy point.

4.7 Other Hardware

The wavelength of the OPO signal wave was measured by a Burleigh WA–4500 pulsed wavemeter in order to calibrate the OPOs. The OPO linewidth was measured by a Burleigh PLSA–3500 pulsed laser spectrum analyzer.

The OPO pulse energy was measured by a Newport model 818J–25 pyroelectric energy meter detector. Pulse energies of the excimer laser and Nd:YAG lasers were measured by a Newport model 818T–150 high power thermopile detector. The outputs of both detectors were read with a Newport model 1825–C power/energy meter.

Two Stanford Research Systems DG535 pulse/delay generators were used to trigger all devices used in the experiments and to set the appropriate delay times. All delay generator parameters could be controlled from a PC via a GPIB interface.

A GaGe CompuScope 85G digital oscilloscope PC plug-in card was used to read the signal from both mass spectrometer detectors. A GaGe CompuScope 1450 digital oscilloscope card was used to read the signal from the pyroelectric detector that measured the OPO pulse energy. Both cards were plugged into PCI slots of a personal computer and were controlled by software described at length in Appendix C. A Tektronix TDS 210 digital oscilloscope was used to monitor the discharge voltage and current profiles, and was accessible from a PC via a GPIB interface.

4.8 Data Acquisition

The data acquisition for all experiments was conducted by the PC that also controlled all necessary devices. The following was installed in the PC: both GaGe oscilloscope cards, a National Instruments PCI–GPIB card for remote control of GPIB devices, and a Precision MicroControl DCX-PC100 card for OPO wavelength tuning.

Software written for these experiments remotely controlled both delay generators and laser delays, read out the TOF mass spectra and OPO pulse energy traces from oscilloscopes, and analyzed the data, saving the spectrum to a file on the PC hard drive.

4.8.1 Blake Group Spectroscopy Tools Software

The Blake Group Spectroscopy Tools (BGSpecT) is designed to be a multipurpose spectrometer software package. For flexibility, it has a modular structure. On the device module level it performs the remote control (GPIB, RS232, PC plug-in cards) of numerous devices that are used in the experiment. For example, when scanning a spectrum, BGSpecT tunes the laser wavelength and reads the signal from a digital oscilloscope. A separate spectrometer module uses the device modules to perform the actual scan. The advantage of such a system is that the spectrometer module does not need to know any device-specific commands (differences between the models of the same device type, etc.) since it works at a higher software level. Thus, the spectrometer module can be used for different experiments simply by changing the software configuration, but not the code behind it.

The device modules may be used to control devices independently, almost as if the user was turning knobs on the device itself. In addition, they allow communication with multiple devices of the same kind. For example, reading the waveforms from multiple 2-channel oscilloscopes simultaneously is essentially the same as reading them from one 4- or

8-channel oscilloscope. In some cases, this helps to conduct affordable experiments with the existing equipment.

BGSpecT is written and compiled in Microsoft Visual Basic. When the modules were first coded, the available computers were slow and there was a noticeable speed difference between software designed in LabView and Basic or C++. Nowadays, the bottleneck is usually in the speed of the experiment itself or the data transfer from the device to the computer. Historically, Visual Basic was used to ensure interoperability with other software developed by the group.

4.8.2 Choice of Delay Times

It was important to carefully select delay times for experimental synchronization. First, since protonation was performed in a hydrogen discharge (4.2), it was necessary to adjust the delay time between the valve opening (discharge start) and ion extraction to maximize the intensity of the protonated ion peak. The long term stability of this signal was ensured by first 'seasoning' the discharge for 0.5 – 1 hour. Usually, ions produced in the beginning of the discharge were used. The ion beam was then intercepted with an intense pulse from the excimer laser (λ = 193 nm, E = 25 – 35 mJ/pulse, 10×15 mm spot size) to dissociate the molecular ions. The delay time for the excimer laser was adjusted to maximize the photodissociation of ions of a selected mass, usually protonated PAHs. This delay then was fixed.

When an OPO was used to scan the spectrum, the delay time for the OPO pump Nd:YAG laser was adjusted for optimum temporal overlap with the excimer pulse as measured by a fast photodiode.

During the spectral scan, the ion signal without the laser was collected as well, nearly in real time. For each OPO wavelength, the MCP signals with the laser was acquired. The laser delay time was then increased by more than 50 μs (longer than the mass spectrum time range) and the 'background' signal was acquired. Finally, the laser delay was returned to its original position.

Typical delay generator parameters were:

Delay generator #1. Internal triggering mode at 5 Hz rate.

$$\begin{cases} \mathrm{T_0} = 0\ \mu\mathrm{s} & , \text{ open pulsed valve (400 } \mu\text{s)} \\ \mathrm{A} = \mathrm{T_0} + 320.00\ \mu\mathrm{s} & , \text{ turn discharge On; trigger delay generator \#2;} \\ & \quad \text{trigger Tektronix TDS 210 oscilloscope (discharge monitor)} \\ \mathrm{B} = \mathrm{A} + 460.00\ \mu\mathrm{s} & , \text{ turn discharge Off} \\ \mathrm{C} = \mathrm{D} - 260.00\ \mu\mathrm{s} & , \text{ turn Coherent Infinity Nd:YAG lamp On} \\ \mathrm{D} = \mathrm{A} + 198.61\ \mu\mathrm{s} & , \text{ turn Coherent Infinity Nd:YAG Q-switch On (OPO);} \\ & \quad \text{trigger GaGe CS 1450 oscilloscope (OPO pulse energy)} \end{cases}$$

Delay generator #2. External triggering mode, triggered by delay generator #1.

$$\begin{cases} \mathrm{T_0} = 0\ \mu\mathrm{s} & \text{– from DG \#1, line A} \\ \mathrm{A} = \mathrm{B} - 1.09\ \mu\mathrm{s} & , \text{ trigger Lambda Physik excimer laser} \\ \mathrm{B} = \mathrm{C} + 18.54\ \mu\mathrm{s} & , \text{ actual excimer pulse produced, for protonated anthracene} \\ \quad 20.13\ \mu\mathrm{s} & , \text{ for protonated pyrene} \\ \quad 12.56\ \mu\mathrm{s} & , \text{ for protonated benzene} \\ \mathrm{C} = \mathrm{T_0} + 180.00\ \mu\mathrm{s} & , \text{ TOF MS ion extraction pulse On (7 } \mu\text{s)} \\ \mathrm{D} = \mathrm{C} + 0.35\ \mu\mathrm{s} & , \text{ trigger GaGe CS 85G oscilloscope (TOF MS spectra)} \end{cases}$$

When the cluster discharge source was used (4.3), there was an additional pulsed valve to trigger. In that case, typical delay times were:

Delay generator #1. Internal triggering mode at 10 Hz rate.

$$\begin{cases} T_0 = 0\ \mu s & , \text{ send to TTL frequency divider, to trigger delay generator \#2} \\ A = B - 0.95\ \mu s & , \text{ trigger Lambda Physik excimer laser} \\ B = D + 0.47\ \mu s & , \text{ actual excimer pulse produced} \\ C = D - 120.00\ \mu s & , \text{ turn Spectra–Physics GCR Nd:YAG lamp On} \\ D = T_0 + 789.44\ \mu s & , \text{ turn Spectra–Physics GCR Nd:YAG Q-switch On (OPO)} \end{cases}$$

Delay generator #2. External triggering mode, triggered by TTL frequency divider at 0.91 (10/11) Hz.

$$\begin{cases} T_0 = 0\ \mu s & , \text{ open } H_2O \text{ pulsed valve (400 } \mu s) \\ A = T_0 + 280.00\ \mu s & , \text{ open discharge pulsed valve (400 } \mu s) \\ B = C + 240.00\ \mu s & , \text{ TOF MS ion extraction pulse On (7 } \mu s); \\ & \quad \text{trigger GaGe CS 1450 oscilloscope (OPO pulse energy)} \\ C = A + 250.00\ \mu s & , \text{ turn discharge On (1200 } \mu s); \\ & \quad \text{trigger Tektronix TDS 210 oscilloscope (discharge monitor)} \\ D = B + 0.35\ \mu s & , \text{ trigger GaGe CS 85G oscilloscope (TOF MS spectra)} \end{cases}$$

4.8.3 Data Analysis

Raw data were processed by the software as soon as it was acquired. After each discharge pulse, the oscilloscope traces were read by the software and then analyzed. For the mass spectra, there was always a mass peak produced by the discharge whose intensity could be monitored. For example, while recording the cluster photodissociation spectrum, the intensity of the protonated PAH peak was monitored. The dynamic range option from the Oscilloscope panel of BGSpecT was used to make sure that the intensity of the desired peak from each shot was within a user selected range. If the signal at that mass was too weak (too few ions) or too strong (saturated), all data from that shot were discarded. 'Good' traces were then averaged, typically up to 60 or 100 traces per wavelength. Averaged mass spectra were then baselined by subtracting a linear fit and saved onto the hard drive for the future analysis, if needed.

The signal for mass spectra was the area under a peak of selected mass. A few masses could be monitored simultaneously. For the OPO pulse energy, the signal was the difference between the maximum and the minimum of the pyroelectric detector signal.

The results were saved into an ASCII file with several columns: laser wavelength, laser pulse energy, and one column per each monitored mass peak. Two files were created: one for the data with the laser, and one without.

After the scan was completed, the data underwent further manual processing. For the neutral dissociation product peak, the value without the laser was subtracted from the value with the laser to improve the baselining. The parent ion and neutral product peaks were then normalized by the parent signal in the absence of the laser to adjust for long term discharge source intensity fluctuations, and then normalized by the OPO pulse energy to yield a final spectrum.